Journal of Sedimentary Research

Journal of Sedimentary Research, 2020, v. 90, 1128–1138
Research Article
DOI: 10.2110/jsr.2020.020

SIMILARITIES AND CONTRASTS BETWEEN THE SUBAERIAL AND SUBAQUEOUS DEPOSITS OF SUBAERIALLY TRIGGERED DEBRIS FLOWS: AN ANALOGUE EXPERIMENTAL STUDY

TJALLING DE HAAS,[1] NIKOLETA SANTA,[1] SJOUKJE I. DE LANGE,[1] AND SHIVA P. PUDASAINI[2]
[1]*Department of Physical Geography, Utrecht University, Utrecht, The Netherlands*
[2]*Institute of Geosciences, Geophysics Section, University of Bonn, Bonn, Germany*
e-mail: t.dehaas@uu.nl

ABSTRACT: **Debris flows and lahars are dense masses of water and sediment which are common phenomena in mountainous and volcanic regions, respectively. Where these flows debouch into water bodies they can trigger impulse waves (tsunamis) and form subaqueous deposits. Such deposits are important indicators for areas at risk from debris flows, lahars, and tsunamis and form archives of past environmental conditions. Correctly interpreting this archive, however, depends on our understanding of the sedimentology and architecture of the deposits. While subaerial debris-flow deposits have been extensively studied, there is a comparative lack of understanding of the deposits of subaerial debris flows that debouch into a water body. We experimentally investigate the similarities and contrasts between subaerial and subaqueous debris-flow deposits for flows of various magnitudes and compositions initiated in a subaerial environment. We show that flows depositing on a subaqueous plane generally have a deposit area similar to flows forming in a subaerial setting. Deposits forming on a subaqueous plane, however, are typically shorter and wider with similar thickness, as a result of interactions between the flow and the reservoir water body. Both in subaerial and subaqueous environments the deposits form coarse-grained lateral levees and frontal snout margins. However, where the levees are able to laterally confine the subaerial flows leading to deposits with constant to tapering width, the subaqueous deposits widen with distance offshore because of flow fluidization. Moreover, the frontal snout is often very dispersed, a sharp frontal margin is absent, and many isolated particles are deposited in front of the main deposit margin as a result of interactions between the debris flow and the reservoir water body. These results largely agree with observations of subaqueous pyroclastic-flow deposits. The similarity in area of subaerial and subaqueous deposits suggests that we can apply empirical relations based on subaerial flows to estimate the inundation area and flow volume of subaerial–subaqueous flows.**

INTRODUCTION

Debris flows and lahars, which are debris flows originating on volcanoes (e.g., Iverson et al. 1998), are common phenomena in mountainous and volcanic regions, respectively. They consist of dense masses of water, soil, and rock (Costa 1988; Iverson 1997), which can erode mountainsides, inundate channels, floodplains, and alluvial fans, and are a major hazard for people and infrastructure (e.g., Jakob 2005). Where debris flows and lahars debouch into water bodies, such as oceans, seas, and mountain lakes, they can trigger impulse waves (tsunamis) with hazardous effects on nearby communities (e.g., Wang et al. 2004; Higman et al. 2018; Heidarzadeh et al. 2019).

Debris flows and lahars generally deposit on moderate slopes in the range of 5–15°, although rare deposits are found on lower and higher slopes (Blikra and Nemec 1998; Blair and McPherson 2009). The deposits of historic flows are important indicators for areas at risk from debris flows, lahars, and tsunamis. Moreover, they form archives of past environmental conditions (e.g., Dühnforth et al. 2007; Schürch et al. 2016; D'Arcy et al. 2017; De Haas et al. 2018a). The extent to which we can interpret the debris-flow deposit archive depends on our understanding of the sedimentology and architecture of debris-flow deposits across the wide range of conditions and environments in which they occur.

While there is a relative wealth of studies on subaerial debris-flow and lahar deposits (e.g., Hubert and Filipov 1989; Blair and McPherson 1994; Iverson et al. 1998; Kim and Lowe 2004; De Haas et al. 2015a), there is a comparative lack of studies and understanding of the subaqueous deposits of subaerial debris flows and lahars that debouched into standing bodies of water (e.g., Trofimovs et al. 2006; Le Friant et al. 2009). Our understanding of subaerial debris-flow deposits stems from both field investigations (Hubert and Filipov 1989; Blair and McPherson 1998; Kim and Lowe 2004) and physical-scale experiments (Major 1997; Major and Iverson 1999; De Haas et al. 2015a). In planform, these flows often form elongated deposits, with coarse-grained lateral levees and snouts (e.g., Kim and Lowe 2004; Blair and McPherson 1998; Johnson et al. 2012; De Haas et al. 2015b, 2015c; Pudasaini and Fischer 2020). In stratigraphy, subaerial debris-flow deposits are generally internally massive, comprising cobbles and outsized boulders randomly dispersed and generally randomly oriented in a finer matrix (e.g., Fisher 1971; Major 1997; Blikra and Nemec 1998; Blair and McPherson 2009; De Haas et al. 2014, 2015c). The composition of a debris flow exerts a strong control on deposit geometry and sedimentology (Pudasaini and Mergili 2019). De Haas et al. (2015a) found that deposit geometry is largely controlled by debris-flow composition: the

Published Online: September 2020
 1527-1404/20/090-1128

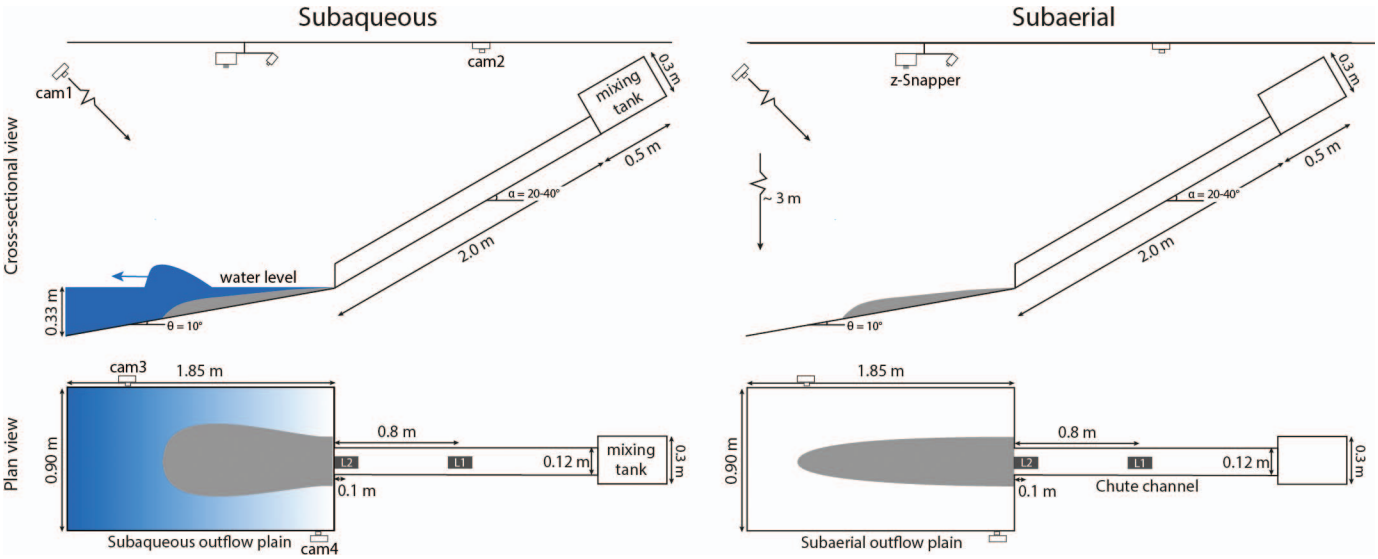

FIG. 1.—Overview of the experimental setup. The debris flow is released from mixing tank and flows via the chute channel onto the subaqueous (left) or subaerial (right) outflow plane. Cam, camera; L, laser. Extended from de Haas et al. (2015a) and from de Lange et al. (2020).

coarse-grained, clay, and water fractions all have a profound effect on lobe height, lobe width, and levee height.

Most research on subaqueous debris-flow deposits focusses on debris flows that originate in the subaqueous environment, such as on steep delta fronts (e.g., Kurtz and Anderson 1979; Prior et al. 1984; Laberg and Vorren 1995; Clare et al. 2018; Vendettuoli et al. 2019). The deposits of these flows are, however, fundamentally different from those of debris flows and lahars that originate subaerially and debouch into a standing body of water, as a result of the strongly contrasting environments in which they form. Subaerial flows that debouch into water form an impulse wave, with which they can interact for some distance (Mohammed and Fritz 2012; Miller et al. 2017; De Lange et al. 2020), resulting in a unique depositional morphology and sedimentology.

The characteristics of the deposits of mass flows that originate in a subaerial setting and debouch into a sea or lake are currently largely unexplored. There are some recent examples of subaerial landslides entering a standing body of water, forming an impulse wave and subaqueous deposit, such as the Tyndall Glacier (Higman et al. 2018; Dufresne et al. 2018) and Taan Fiord landslides (George et al. 2017) in Alaska. In addition, submarine deposits of subaerially induced landslides and debris avalanches are common on the flanks of volcanic islands (e.g., Urgeles et al. 1997; Mitchell et al. 2002; Schneider et al. 2004; Chun and Lee 2019). The flow conditions of these landslides and debris avalanches are generally unknown, however, such that their deposits cannot be studied in direct reference to the flow conditions that formed them. To date, the only location where subaqueous mass-flow deposits have been studied and for which the subaerial flow conditions are largely known is the Soufrière Hills volcano in Montserrat (DePlus et al. 2001; Hart et al. 2004; Trofimovs et al. 2006, 2008; Le Friant et al. 2009). The present lack of understanding of the subaqueous deposits of mass flows, such as debris flows and lahars, that debouched into a standing body of water hampers their identification and interpretation, inhibiting identification of areas of risk of such flows for tsunami hazard identification and paleo-environmental reconstructions.

Here, we experimentally investigate the similarities and contrasts between subaerial and subaqueous debris-flow deposits for debris flows of various magnitudes and compositions initiated in a subaerial environment. In specific, we compare the dimension and particle-size sorting of deposits that form in a subaerial and subaqueous environment, and provide novel insights into the characteristics of subaqueous deposits generated by debris flows that have been initiated subaerially.

METHODS

To determine the similarities and contrasts between subaerial and subaqueous deposits of debris flows that are initiated in a subaerial environment we performed a series of 94 physical-scale experiments (36 subaerial, 58 subaqueous). For the subaerial experiments we used the flume setup previously described in De Haas et al. (2015a; 2016, 2018b), in which effects of debris-flow composition on debris-flow morphology, autogenic dynamics of debris-flow fans, and effects of debris-flow magnitude-frequency on avulsions and fan development were previously studied, respectively. For the subaqueous experiments, we extended this flume setup with a water basin. The experiments presented here were also used in De Lange et al. (2020), who studied the relation between debris-flow dynamics and impulse-wave generation. Below we describe the experimental setup, the composition of the experimental debris flows, data analyses, and potential scale effects.

Experimental Setup

The experimental setup consisted of a mixing tank placed at the top of a steeply inclined channel with a constant slope (generally 30°, varied between 20° and 40° for a few experiments), connected to a laterally unconstrained outflow plane inclined at 10° (Fig. 1). The channel had a length of 2 m and a width of 0.12 m, while the outflow plane was 1.85 m long and 0.9 m wide. The floor and sides were covered with sandpaper with an average particle diameter 0.19 mm, while roughness on the outflow plane was created by gluing sand to its surface (coarse sand in Fig. 2). Sediment and water were manually mixed for approximately 20 s in the tank for each experiment and then released electromagnetically through an upwards swinging of the opening gate. The same fresh tap water was used for the debris flows and the reservoir. Relatively soft tap water was used (5.4° DH).

For the subaqueous experiments, the water level in the outflow-plane basin matched the downstream end of the channel. The water depth increased linearly with distance from the base of the outflow channel as a

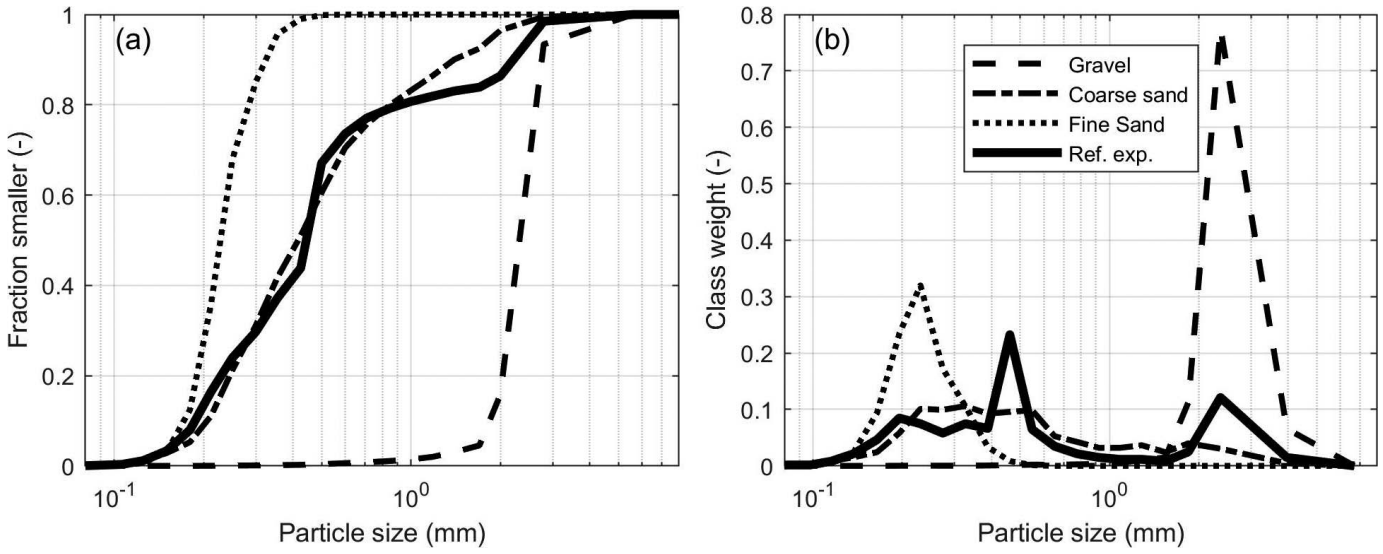

FIG. 2.—**A)** Cumulative particle distribution of the four sediment types (clay excluded) and the reference mixture. **B)** Frequency distribution of the sediment types. Figure modified from De Haas et al. (2015).

result of the 10° basin-floor inclination leading to a water depth of 0.33 m at the downstream end of the basin.

Cameras were used to record debris-flow dynamics (Fig 1). GoPro HERO6 cameras were used to capture a general overview of the experiment (cam1), to extract the debris-flow velocity in the subaerial outflow channel (cam2), and to capture outflow and wave dynamics (cam3–4). The resolution of these cameras was set to 1440 ppi with a frame rate of 60 fps.

Two lasers, L1 (Baumer OADM 20U2480/S14C) and L2 (Baumer FADK14U4470/S14/IO), were used to measure the flow thickness near the middle (1.20 m downslope of the mixer outlet) and the end (1.90 m downslope of the mixer outlet) of the subaerial channel. Debris-flow weight was measured with a circular load cell connected to a plate in the flume floor with a radius of 1.6 cm that was emplaced in the middle of the outflow channel. This load cell was located at a distance of 1.2 m downstream of the outlet of the mixing tank and recorded with a frequency of 100 Hz.

Deposit morphology was measured with a Vialux z-Snapper 3-D scanner that captured a high-accuracy 3-D point cloud from a fringe pattern projector and camera (submillimeter vertical and horizontal accuracy) (Hoefling 2004). Point clouds from the 3-D scanner were converted to a gridded digital elevation model (DEM) of 1 mm resolution through natural neighbor interpolation.

Debris-Flow Composition

The experimental debris flows were composed of water, kaolinite clay, well-sorted fine sand, poorly sorted coarse sand, and basaltic gravel parts of 2–5 mm in diameter (Fig. 2). The clay increased the viscosity of the flow, while the gravel could accumulate at the front of the flow, both mimicking natural debris-flow behavior (De Haas et al. 2015a; De Haas and van Woerkom 2016; De Lange et al. 2020). The reference mixture of 8.0 kg (0.0041 m^3) consisted of 18 vol% gravel, 59 vol% coarse sand, 21 vol% fine sand, 2 vol% clay, and 0.44 vol% water. The volume percentages of particles refer to the volume ratio of solid particles, while the volume percentage of water refers to the volume ratio of both the solid and the liquid phase. Effects of flow volume, composition, and subaerial outflow slope were explored by systematically varying these parameters around the reference flow. Flow volumes varied between 0.0018 and 0.0092 m^3, volumetric water contents between 40 and 60%, volumetric gravel fraction between 0 and 64%, volumetric clay fraction between 0 and 29%, and channel slope varied between 20 and 40° (see supplementary table 1 for a full overview of the experimental conditions for each run). To quantify the natural variability within the flows and its influence on the obtained trends, all experiments were performed at least twice (De Lange et al. 2020).

Quantification of Debris-Flow Deposit Dimensions

The DEMs were used to quantify deposit dimensions (Fig. 3). We manually digitized the extent of the deposits on hillshaded DEMs to determine deposit area. We further used the deposit outline to extract the maximum deposit width and runout. As an objective measure to compare the often heterogeneous deposit thickness between flows, we determined the maximum deposit thickness at a distance of 75% of the total runout of each deposit.

Potential Scale Effects

Small-scale experimental debris flows exhibit disproportionately large effects of yield strength, viscous flow resistance, and grain inertia, while exhibiting disproportionately little effect of pore-fluid pressure (Iverson 1997, 2015; Iverson et al. 2010). Nevertheless, we have previously shown that the large-scale flow patterns and deposits of the subaerial debris flows created in this experimental setup mimic those of natural debris flows (De Haas et al. 2015a, 2016, 2018b). These frictional flows form distinct depositional lobes, and coarse particles are concentrated in coarse-grained lateral levees and snouts (De Haas et al. 2015a, 2016). Moreover, geometrically the experimental debris flows follow the relationships found for natural debris flows (e.g., Iverson 1997; Rickenmann 1999; Bulmer et al. 2002; Griswold and Iverson 2008; Toyos et al. 2007; D'Agostino et al. 2010): channel width-to-depth ratios, and runout length and area relative to debris-flow volume, are similar to those in natural debris flows (De Haas et al. 2015a).

For the subaqueous outflow and deposit formation, as well as impulse-wave generation, De Lange et al. (2020) showed that both the Reynolds (Re) and Froude (Fr) numbers fall within the accurate scaling range defined by Heller et al. (2008) for impulse transfer between subaerial landslides and a water body. Furthermore, inertial forces dominate over surface-tension forces in the impulse wave for all experiments but the smallest-volume ones (Heller 2011; De Lange et al. 2020). Surface tension

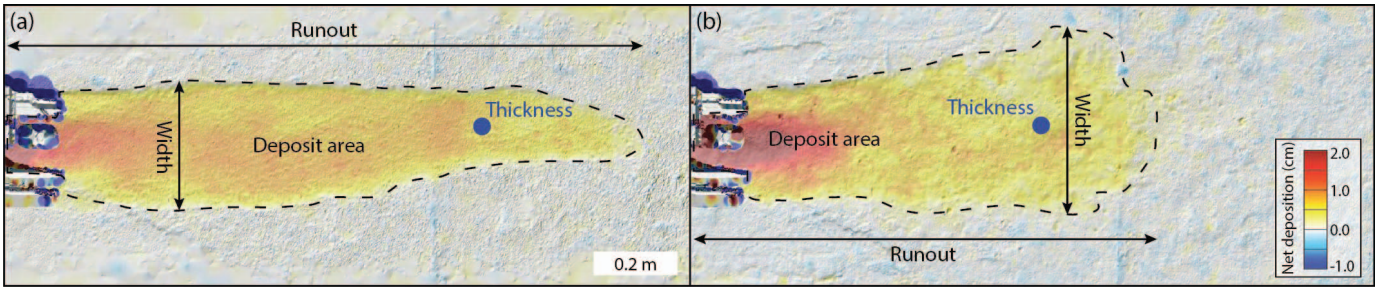

FIG. 3.—Measurements of deposit dimensions. **A)** Runout, deposit area, deposit width, and maximum thickness at 75% of the runout on a subaerial reference experiment (exp. 63 in Supplemental Table 1). **B)** Likewise for a subaqueous reference experiment (exp. 10 in Supplemental Table 1).

accounted for approximately 1% of the total of the wave energy, which is within the limit of traditional scaling rules for experimental waves (Hughes 1993).

We emphasize that the experiments presented here are not intended as 1:1 scaled analogues of subaerial and subaqueous debris-flow deposits, but rather aim to highlight the effects of flow composition on deposit morphology and sedimentology in subaerial and subaqueous deposits. In addition, we focus on identifying the contrasts between debris-flow deposits formed above and below water in otherwise similar experimental settings.

RESULTS

General Flow Conditions

Flow Characteristics in the Channel.—The hydrographs of the experimental debris flows were characterized by a steep front with a typical thickness of approximately 2 cm and a typical duration of approximately 0.5 s (Fig. 4). The mean frontal debris-flow velocity through the channel was on average 2.18 m/s with a standard deviation of 0.31 m/s. The thickness of the debris flow was generally roughly 0.2 cm lower near the channel outflow compared to near the middle of the channel, due to shearing and the time needed for the debris flow to spread out.

Outflow Dynamics.—The majority of the subaerial debris flows segregated into a more resistive gravelly flow front and a finer-grained, more dilute, main body and tail. When the flows reached the lower-angle outflow plane the flows started to decelerate. During deceleration the flow front was continuously shouldered aside into lateral levees by a more dilute and faster-moving flow body (Fig. 5A–D). The formation of lateral levees confined the flow, which enabled the formation of elongate debris-flow deposits. Only in debris flows with a clay fraction exceeding approximately 0.22, viscous forces increasingly dominated over collisional and frictional forces hampering particle segregation, formation of a coarse-grained front, and formation of lateral levees (De Haas et al. 2015a).

Subaqueous outflow differed substantially from subaerial outflow (Fig. 5). When the debris flow entered the water, it pushed the water forward, generating impulse waves. This continued until wave celerity exceeded the subaqueous debris-flow velocity and the wave became detached from the debris flow (see De Lange et al. 2020, for more details on impulse-wave generation). Upon entering the water, fines (clay) partly escaped the debris-flow mixture and were suspended into the water column. The larger grains continued to flow over the floor of the outflow basin. The initial debris-flow front at the time of impact, however, was often partly lifted from the ground, partly suspended, and transported within the leading impulse wave (Fig. 5G).

Because of the suspension of clay into the water column, we could not observe the flow patterns on the subaqueous outflow plane in detail. However, after draining the reservoir we observed that the subaqueous deposits did often show particle segregation with coarse-particle aggregation in lateral levees and near the flow front, showing that flow patterns on the subaqueous outflow plane to varying degrees mimicked those on the subaerial outflow plane. In comparison to the subaerial debris-flow deposits, however, local segregation was less pronounced, and lateral flow constriction was less effective, showing that the levee-formation and particle-segregation mechanisms were less effective in the water basin.

Controls on Deposit Dimensions in a Subaerial and Subaqueous Setting

Flow momentum (mass times velocity) in the channel strongly controlled the dimensions of the flow deposit, both under subaerial and subaqueous conditions (Fig. 6). Generally, a given flow momentum resulted in a similar deposit area under subaerial and subaqueous conditions (Fig. 6A). A few flows with a flow momentum of approximately 20 N.s formed much larger deposit areas under subaerial conditions

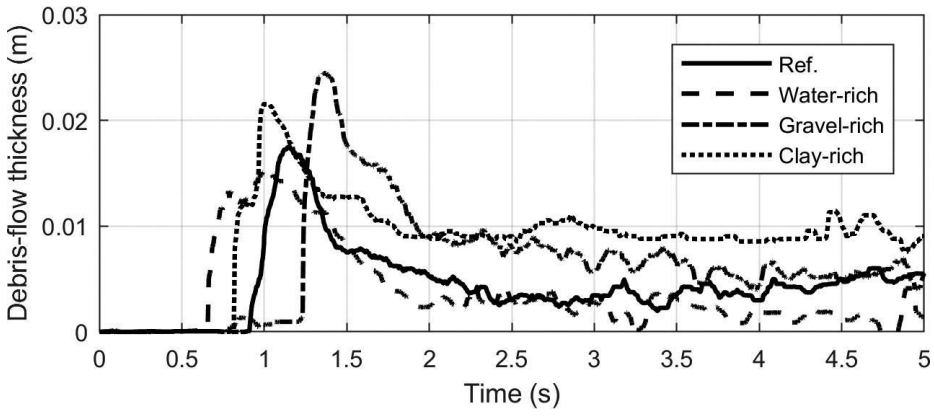

FIG. 4.—Example of debris-flow hydrographs in the channel 1.2 m downstream of the release gate (LS1 in Fig. 1), for a reference experiment (exp. 10 in Supplemental Table 1), a water-rich experiment (exp. 30), a gravel-rich experiment (exp. 39), and a clay-rich experiment (exp. 49). A 0.1 s median filter was applied to the data. See Supplemental Table 1 for experimental details.

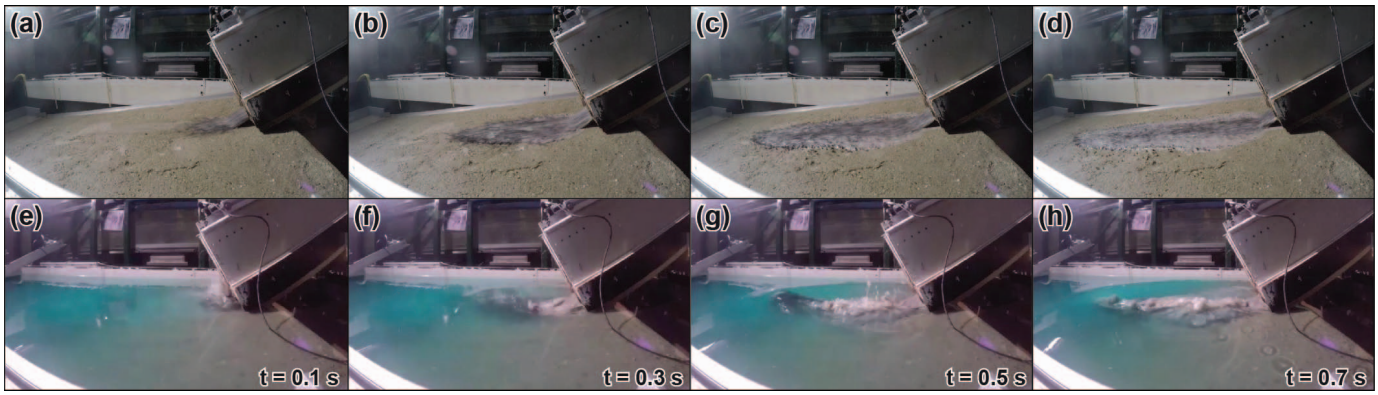

FIG. 5.—Debris-flow deposition in a gravel-rich debris flow in a subaerial (exp. 39 in Supplemental Table 1) **A**–**D)** and subaqueous setting (exp. 79) **E**–**H)** for the same composition and boundary conditions. See Supplemental Table 1 for experimental details. Supplemental Movies show the full outflow dynamics depicted here.

compared to subaqueous conditions. These flows were water-rich (Fig. 7E), as further detailed below. For a given flow momentum, the maximum runout on a subaerial outflow plane generally exceeded the runout on a subaqueous outflow plane (Fig. 6B). In addition, the maximum deposit width on a subaqueous outflow plane was larger than the deposit width on a subaerial outflow plane (Fig. 6C). There was a large variability in deposit thickness for flows of a given momentum, likely as a result of the wide range of flow compositions that were explored, and deposit thickness appeared to be unrelated to flow momentum (Fig. 6D). On a subaqueous outflow plane, deposits were thus generally shorter and wider while deposit area and thickness were similar compared to deposits that formed on a subaerial outflow plane under otherwise similar conditions.

In Figure 7 we break down these results to identify the effects of flow mass, water content, gravel content, clay content, and channel slope. Deposit area, runout, deposit width, and deposit thickness increased with flow mass for both subaerial and subaqueous conditions. There was a tight relation between flow mass and deposit area for both subaerial and subaqueous conditions, and there was no difference in deposit area between subaerial and subaqueous conditions (Fig. 7A). The deposits that formed under subaerial conditions were more elongated, with a longer runout and a smaller maximum width (Fig. 7B, C). Thickness of the deposit at a distance of 75% of the maximum runout was fairly similar, although the deposits appeared to be slightly thicker for a given mass under subaqueous conditions (Fig. 7D).

An increase in volumetric water content in the debris flows resulted in larger deposit area, runout, and maximum deposit width under both subaerial and subaqueous conditions. The runout area was increasingly enhanced in subaerial relative to subaqueous outflow conditions with increasing water content (Fig. 7E). Similarly, the runout distance under subaerial conditions exceeded the runout distance under subaqueous conditions (Fig. 7F). Maximum deposit width, on the other hand, similarly increased with water content under both subaerial and subaqueous conditions (Fig. 7G). The thickness of the deposits at a distance of 75% of the maximum runout appeared to be unaffected by water content under subaqueous conditions, while there was a decrease in thickness with water content for subaerial conditions (Fig. 7H).

The deposit area similarly decreased with increasing gravel content for both subaerial and subaqueous conditions (Fig. 7I). For low gravel contents, deposits under subaerial conditions were longer and smaller than the deposits that formed under subaqueous conditions (Fig. 7J–K). However, towards gravel fractions of approximately 40% and higher, deposit dimensions were similar under both subaerial and subaqueous conditions forming deposits with relatively restricted runout and width. The thickness of the deposits at a distance of 75% of the maximum runout was thicker under subaerial and thinner under subaqueous conditions (Fig. 7L).

There was an optimum clay fraction around 10 vol% at which deposit area, runout, and maximum deposit width were maximal. Deposit area was approximately similar under subaerial and subaqueous conditions (Fig. 7M). The deposits forming under subaerial conditions formed more elongated deposits, with longer (Fig. 7N) and narrower (Fig. 7O) deposits compared to those formed under subaqueous conditions. The thickness of the deposits at a distance of 75% of the maximum runout increased with clay content under both subaerial and subaqueous conditions, but the deposits that formed under subaerial conditions were generally thicker than those formed under subaqueous conditions (Fig. 7P).

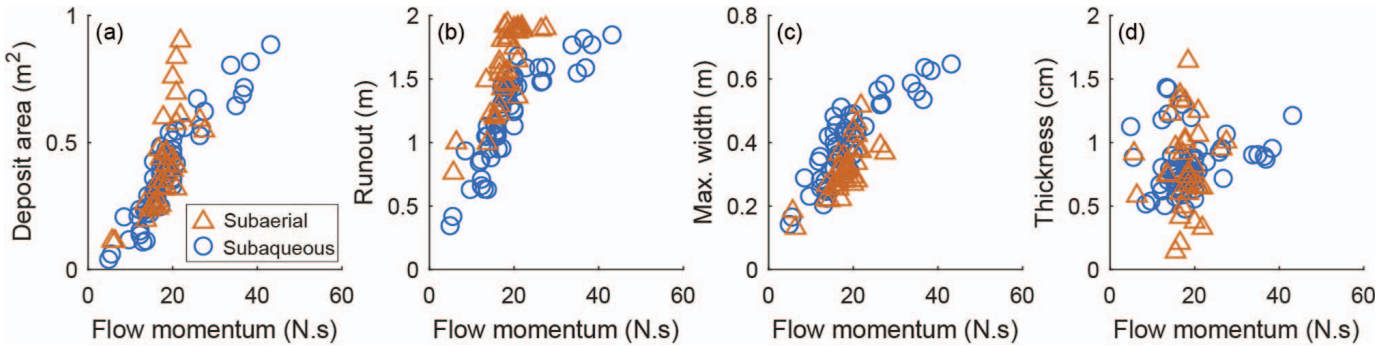

FIG. 6.—Relation between flow momentum in the channel and **A)** deposit area, **B)** runout distance on the outflow plane, **C)** maximum deposit width, and **D)** deposit thickness at 75% of the maximum runout. Note that length of the outflow plane 1.85 m, limiting maximum deposit area and runout for some flows. See Supplemental Table 1 for experimental details.

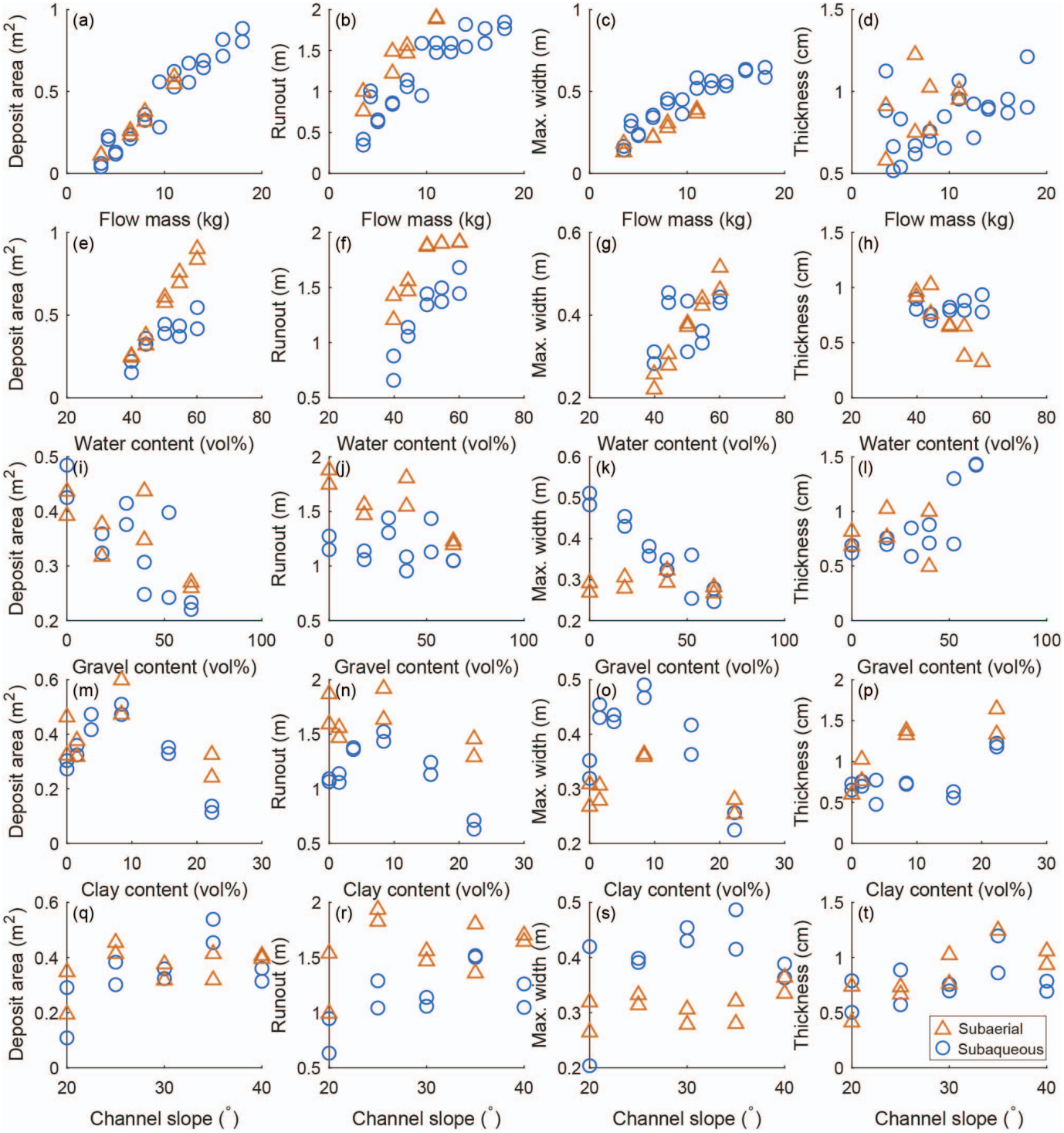

FIG. 7.—Overview of the effect of **A–D)** flow mass, **E–H)** water content, **I–L)** gravel content, **M–P)** clay content, and **Q–T)** channel slope on deposit area, runout distance on the outflow plane, maximum deposit width, and deposit thickness at 75% of the maximum runout. Note that length of the outflow plane 1.85 m, limiting maximum deposit area and runout for some flows. See Supplemental Table 1 for experimental details.

An increase in channel slope from 20° to 25° resulted in an increase in deposit area, while for steeper channels deposit area appeared to be unrelated to channel slope (Fig. 7Q). Similarly, runout, maximum deposit width, and thickness of the deposits at a distance of 75% of the maximum runout appeared largely unrelated to channel slope (Fig. 7R–T). We tentatively attribute this counterintuitive finding to the sharp transition in slope between the channel and outflow plane, which caused increasing initial local lateral spreading, and thereby momentum loss, at the transition from channel to outflow plane for increasing differences in channel and outflow-plane slope. There was no difference in deposit area between

FIG. 8.—Photograph highlighting grain-size sorting in selected subaerial debris flows. The coarse-grained gravel particles have a black color, the sand is brown, while the clay has a white color. **A–C)** Debris flows with an increasing volume and mass of 3.5 kg (exp. 59 in supplementary table 1), 8.0 kg (exp. 63), and 11.0 kg (exp. 65), respectively. **D–F)** Debris flows with an increasing volumetric water content of 40% (exp. 68), 50% (exp. 69), and 60% (exp. 74), respectively. **G–I)** Debris flows with an increasing gravel content of 0% (exp. 76), 39% (exp. 78), and 64% (exp. 80), respectively. **J–L)** Debris flows with an increasing clay content of 0% (exp. 81), 11% (exp. 84), and 29% (exp. 85), respectively. Boundary conditions for the subaerial flows shown here match those shown in for subaqueous flows shown in Figure 9. Note the changing perspective between photographs. See Supplemental Table 1 for experimental details.

subaerial and subaqueous conditions, while the subaerial deposits were longer and narrower than the subaqueous deposits. The thickness of the deposits did not differ between deposits formed in subaerial and subaqueous conditions.

Particle-Size Sorting in Subaerial and Subaqueous Deposits

The subaerial deposits generally consisted of a channel bordered by elevated lateral levees grading into a frontal snout (Fig. 8). The coarsest, gravel, particles were concentrated in the lateral levees and frontal snout margins. The middle of the deposits was substantially finer grained, consisting predominantly of sand and clay. This general particle-sorting pattern was consistently present for all tested flow sizes and water contents (Fig. 8A–F). An increase in gravel content resulted in increasingly distinct levees both in dimensions and particle size. The increase in gravel content led to a larger accumulation of coarse particles at the front of the flow, and therefore larger and coarser-grained lateral levees and frontal snout margins (Fig. 8G–I). For the largest gravel contents, the frontal snout margins consisted almost purely of gravel forming an open textured deposit (Fig. 8I). Large amounts of clay, on the other hand, hampered particle interactions, sorting, and grain-size segregation, resulting in an absence of coarse-grained lateral levees and frontal snout margins (Fig. 8J–L).

In the subaqueous deposits coarse-grained lateral levees were also formed, although typically less pronounced compared to the subaerial deposits, and generally also becoming less well-developed with runout distance (Fig. 9). Where the lateral levees were able to laterally confine the subaerial deposits, in most of the subaqueous deposits this was less

FIG. 9.—Photograph highlighting grain-size sorting in selected subaqueous debris flows. The coarse-grained gravel particles have a black color, the sand is brown, while the clay has a white color. **A–C)** Debris flows with an increasing volume and mass of 3.5 kg (exp. 2 in Supplemental Table 1), 8.0 kg (exp. 10), and 11.0 kg (exp. 13), respectively. **D–F)** Debris flows with an increasing volumetric water content of 40% (exp. 24), 50% (exp. 25), and 60% (exp. 30), respectively. **G–I)** Debris flows with an increasing gravel content of 0% (exp. 32), 39% (exp. 35), and 64% (exp. 39), respectively. **J–L)** Debris flows with an increasing clay content of 0% (exp. 42), 11% (exp45), and 29% (exp. 50), respectively. Boundary conditions for the subaqueous flows shown here match those shown in for subaerial flows shown in Fig. 8. Note the changing perspective between photographs. See Supplemental Table 1 for experimental details.

effective and the deposits gradually became wider with runout distance. Coarse-grained gravel particles were concentrated in the frontal margins of the subaqueous deposits, but the frontal depositional snout was much more spatially dispersed compared to the distinct snout in the subaerial deposits. The frontal snout of the subaqueous deposits was generally widely spread out. In addition, in front of the main frontal snout large numbers of isolated gravel particles were deposited, especially in large volume and water-rich flows (Fig. 9A–F). This effect was limited in the flows with large gravel contents, in which the frontal snout was hardly more dispersed compared to that in subaerial conditions and the deposit dimensions were relatively similar (Fig. 9I). This indicates that the impact momentum of such gravel-rich flows could not substantially disperse the frontal assembly of gravel, which thus remained intact. For the clay-rich flows we observed a veneer of clay particles deposited throughout the basin, as a result of the suspension of large amounts of clay into the water column (Fig. 9K). In the flows with very large clay contents, exceeding 20%, we observed no grain sorting and grain-size segregation, as was also the case under subaerial conditions.

DISCUSSION

Similarities and Contrasts Between Subaerial and Subaqueous Debris-Flow Deposits

Our results show that debris flows that are initiated in a subaerial environment but debouch into and deposit onto a subaqueous plane generally have a deposit area roughly similar to that of debris flows with the same volume and composition forming in a fully subaerial setting. The shape of the deposit does differ, however, with the deposits forming in a subaqueous setting being shorter and wider while the thickness of the

deposit is generally similar. This is the result of interfacial drag between the debris flow and the water body, and also other momentum exchanges such as buoyancy and virtual mass (Pudasaini 2012, 2019, 2020; Pudasaini and Mergili 2019). Particularly, the drag results in slowing down of the flow in the forward direction, pushing and expanding the debris mass in the lateral direction due to lateral shearing (Kafle et al. 2019), leading to a reduced runout and larger width in subaqueous settings.

The elongated subaerial debris-flow deposits generally form coarse-grained levees and frontal snout margins, except in flows with high clay contents exceeding approximately 20% wherein the large viscosity inhibits particle interactions, sorting, and grain-size concentration. This was also experimentally observed by De Haas et al. (2015a), which is unsurprising given the similar flume setup and flow composition and the strong reproducibility of these types of experiments (Adams et al. 2019). Such phenomena have also been simulated by Pudasaini and Fischer (2020) with their two-phase mechanical model for phase separation. Grain sorting and size segregation was also evident in the subaqueous deposits, which generally also form coarse-grained lateral levees and frontal snout margins. However, where the levees are able to laterally confine the subaerial flows leading to deposits that generally have a constant or tapering width, the subaqueous deposits generally become increasingly wide with runout distance. Moreover, the frontal snout is often very dispersed. This is the result of the state of the debris material at the time of impact, the impact momentum, momentum transfer between the debris and the reservoir, and the sudden amplification of the fluid fraction in the subaqueous debris material (Pudasaini 2012, 2014; Pudasaini and Mergili 2019), resulting in fluidization that led to a quick dispersion of the solid particles in the reservoir.

The observed differences between debris-flow deposits forming in a subaerial and a subaqueous environment can be explained by the processes that operate when a subaerial debris flow debouches into a water basin. Upon entering the basin, the debris flows pushed the water forward, forming an impulse wave. The debris-flow front remained connected to the impulse wave, still pushing it forward, until the wave celerity exceeded the subaqueous debris-flow velocity and the wave was detached. Wave detachment generally occurred around a distance of 0.50–0.85 m from the channel outlet, corresponding to a water depth of 0.08–0.15 m (De Lange et al. 2020). The frontal particles of the debris flow, often consisting of an accumulation of coarse-grained gravel particles, generally became partly suspended by and entrained by the impulse wave. These particles settle only after the debris flow detached from the impulse wave. This process, also due to relatively large vertical acceleration of particles, caused the dispersion of the debris-flow front and explains the large area in front of the deposit where isolated gravel particles were found. In front of subaqueously triggered fine-grained debris flows isolated blocks of sediment can be found downslope of the deposit edge, termed outrunner blocks (Prior et al. 1984). Our results highlight that outrunner blocks found in proximal settings might not result only from subaqueously triggered debris flows but can also stem from debris flows triggered in a subaerial setting.

Lateral levees are formed in subaerial debris flows by pushing of the faster-moving, more dilute, finer-grained flow body against the slower-moving flow front rich in coarse-particles (Johnson et al. 2012; Pudasaini and Fischer 2020). This causes the frontal particles to be shouldered aside and be deposited at the static margin of the flow, simultaneously forming a corridor for the flow body to reach the flow front at high velocities. The lateral levees observed in the subaqueous deposits show that similar processes occur in subaqueous environments. However, the dispersion of the flow front by the impact, fluidization, impulse wave, and the larger deceleration of the flow front due to the momentum transfer between the debris and water basin makes levee formation less effective and forces the flow to spread laterally, forming shorter and wider deposits.

Interestingly, the dimensions and particle-size sorting in gravel-rich debris flows were very similar between subaerial and subaqueous deposits. We relate this to the relatively low momentum of these flows as a result of the large accumulation of coarse particles at the flow front decelerating the flow due to high grain friction. This results in a relatively weak impulse wave not able to substantially suspend the coarse grains at the flow front. In contrast, the large-volume and water-rich flows have higher momentum, generating large impulse waves (De Lange et al. 2020) that are able to strongly suspend and disperse the frontal accumulation of large particles, explaining the strongly dispersed frontal deposits of these flows (Fig. 9).

Our results show that flow composition strongly controls deposit dimensions and sedimentology in both subaqueous and subaerial deposits, although to different degrees. The effects of composition on the subaqueous debris-flow deposits established here may help the interpretation of deposits from subaerially initiated debris flows, lahars, pyroclastic flows, and debris avalanches which have been reported to produce subaqueous deposits that strongly vary in composition (e.g., DePlus et al. 2001).

Comparison to the Submarine Deposits of Pyroclastic Flows

There is a lack of studies that connect subaerial mass-flow conditions to the resulting subaqueous deposit characteristics in nature. The July 2003 pyroclastic flow originating from the Soufrière Hills volcano in Montserrat provides a positive exception (Deplus et al. 2001; Hart et al. 2004; Trofimovs et al. 2006, 2008; Le Friant et al. 2009). Pyroclastic flows are dense flows of sediment supported by hot gas, which exhibit flow dynamics and sorting roughly similar to debris flows despite having gas instead of water as interstitial substance. At the Soufrière Hills volcano the subaqueous deposits were studied in direct reference to the subaerial flow conditions (Trofimovs et al. 2006). The July 2003 pyroclastic flow entered the sea as a thick and dense flow with an estimated velocity of 10–15 m/s (Herd et al. 2006). The event formed two lobate deposits extending roughly 5 km offshore. The lateral lobe margins were steep-sided with well-defined margins, whereas the frontal regions gradually decreased in thickness. Moreover, the deposit gradually widened with distance offshore (Trofimovs et al. 2006). The tens-of-meters-thick proximal deposits had a massive, poorly sorted, coarse-grained, and fines-depleted texture. Offshore of the massive deposit, a thin layer ($<$ 1 m) of well-sorted deposits was composed predominantly of sand and silt (Trofimovs et al. 2006, 2008). Based on our experiments, we can postulate that these observations show that the coarse particles in the pyroclastic flow were retained in the basal parts of the flow, while the fine ash particles were mixed into the water. The abrupt lateral margins of the proximal lobe and the absence of finer deposits beyond these margins indicate that the pyroclastic flows continued to behave as a granular mass flow after entering the sea (Trofimovs et al. 2006). The proximal part of the deposits, which behaved as a granular mass flow, was deposited on 7–10° gradients. These gradients are similar to the gradients on which subaerial coarse-grained pyroclastic flows are deposited (e.g., Sparks et al. 1997; Macías et al. 1998).

The behavior of this pyroclastic flow as it entered the sea as well as the resulting deposit has much in common with the small-scale experimental subaqueous debris-flow deposits observed here. We also found that: 1) the flow continued to behave as a debris flow in the subaqueous environment, forming a thick lobe with well-defined lateral margins and a massive, poorly sorted texture; 2) deposit width increased with distance offshore; 3) deposit thickness decreased with distance offshore; 4) the angle of deposition did not vary much between a subaerial and subaqueous setting, although we did find a slight decrease in mobility within the subaqueous domain; and 5) fines effectively escaped the mass-flow mixture into the highly turbulent water column after the mass flows entered the water. These fines may have formed a turbidity current, which could however not fully

develop in our experimental setup because of the limited longitudinal extent of our water basin.

Implications for Flow Volume Reconstruction from Subaqueous Debris-Flow Deposits

Multiple authors have shown that there is a relation between debris-flow volume and inundation area (e.g., Iverson et al. 1998; Rickenmann 1999; Berti and Simoni 2007; Griswold and Iverson 2008; Pudasaini and Miller 2013). Our finding that the subaerial and subaqueous depositional areas formed by subaerially triggered debris flows are generally similar suggests that these empirical relations might also be applied to estimate the inundation area of subaqueous debris-flow deposits. In addition, Berti and Simoni (2007) present an empirical relation between flow volume and deposit thickness, which might also be applicable to subaqueous debris-flow deposits as our results indicate that deposits often have similar thickness in subaerial and subaqueous settings. Such relations could be used to reconstruct the volumes of mass flows from their deposition area on the seafloor, such as for example offshore the Soufrière Hills Volcano in Montserrat (Deplus et al. 2001; Hart et al. 2004; Trofimovs et al. 2006, 2008; Le Friant et al. 2009). In addition, these empirical relations could provide rough estimates of flow volumes from the thickness of subaqueous debris-flow deposits in stratigraphy (e.g., Sohn et al. 2008).

CONCLUSIONS

A series of physical scale experiments was performed to study the similarities and contrasts of subaerial and subaqueous deposits of debris flows that are initiated in a subaerial setting. The effects of flow magnitude, composition, and channel slope on the dimensions and particle-size sorting of subaerial and subaqueous deposits were analyzed in detail.

The debris-flow deposit area in a subaerial and subaqueous environment was generally similar. In a subaqueous environment the deposits were generally shorter and wider, however, while the thickness of the deposits was roughly similar. Both grain-size segregation and particle fluid separation, leading to deposits with relatively coarse-grained lateral levees and frontal snout margins, were evident in most of the subaerial and subaqueous deposits. In the subaerial setting, the levees were able to laterally confine the subaerial flows, forming deposits with a constant to tapering width. In contrast, the subaqueous deposits became wider with runout distance. Furthermore, the frontal snout was often very dispersed, a sharp frontal margin was absent, and many isolated particles were deposited in front of the main deposit margin. This was the result of momentum transfer during debris impact on the water body and formation of impulse waves, which was able to suspend and entrain the particles at the front of the debris flows, dispersing the debris-flow front.

The experiments presented here provide a framework for the interpretation of the morphology, sedimentology, and architecture of historical subaqueous debris-flow and lahar deposits, which may help identification of subaqueous debris-flow deposits and thereby areas at risk from such flows. The similarity in subaerial and subaqueous deposit area and thickness suggest that empirical relations between inundation area, flow thickness, and flow volume based on subaerial mass flows might also be applied to subaerially triggered mass flows forming subaqueous deposits. Such relations could be applied to reconstruct the volumes of mass flows from their depositional area or architecture on the sea floor.

SUPPLEMENTAL MATERIAL

Supplemental Table 1 is available from the SEPM Data Archive: https://www.sepm.org/supplemental-material.

ACKNOWLEDGEMENTS

This research has been financially supported by the German Research Foundation (DFG), project Nr. PU 386/5-1: "A novel and unified solution to multi-phase mass flows: U_MultiSol" granted to SP and TdH. The experiments were performed as part of the MSc thesis projects of NS and SdL, supervised by TdH. We thank Arjen van Eijk and Bas van Dam, lab technicians at Utrecht University, for their help with flume construction and installation of measurement devices.

REFERENCES

Adams, K., Wasklewicz, T., De Haas, T., Lecce, S., and Gares, P., 2019, Reproducibility of debris-flow fan physical modeling experiments: Colorado School of Mines, Environmental and Engineering Geologists, Special Publication 28.

Berti, M., and Simoni, A., 2007, Prediction of debris flow inundation areas using empirical mobility relationships: Geomorphology, v. 90, p. 144–161.

Blair, T.C., and McPherson, J.G., 1994, Alluvial fans and their natural distinction from rivers based on morphology, hydraulic processes, sedimentary processes, and facies assemblages: Journal of Sedimentary Research, v. 64, p. 450–489.

Blair, T.C., and McPherson, J.G., 1998, Recent debris-flow processes and resultant form and facies of the Dolomite alluvial fan, Owens Valley, California: Journal of Sedimentary Research, v. 68, p. 800–818.

Blair, T.C., and McPherson, J.G., 2009, Processes and forms of alluvial fans, *in* Parsons, A., and Abrahams, A., eds., Geomorphology of Desert Environments: The Netherlands, Springer, p. 413–467.

Blikra, L.H., and Nemec, W., 1998, Postglacial colluvium in western Norway: depositional processes, facies and palaeoclimatic record: Sedimentology, v. 45, p. 909–960.

Bulmer, M.H., Barnouin-Jha, O.S., Peitersen, M.N., and Bourke, M., 2002, An empirical approach to studying debris flows: implications for planetary modeling studies: Journal of Geophysical Research, v. 107, p. 1–16.

Chun, J.H., and Lee, H.J., 2019, Subaerial and subaqueous investigations of volcanic debris avalanche and lahar deposits on the northern coast of Ulleung Island, Korea: Journal of Coastal Research, v. 90, p. 369–376.

Clare, M.A., Le Bas, T., Price, D.M., Hunt, J.E., Sear, D., Cartigny, M.J., Vellinga, A., Symons, W., Firth, C., and Cronin, S., 2018, Complex and cascading triggering of submarine landslides and turbidity currents at volcanic islands revealed from integration of high-resolution onshore and offshore surveys: Frontiers in Earth Science, v. 6, p. 223.

Costa, J.E., 1988, Rheologic, geomorphic, and sedimentologic differentiation of water flood, hyperconcentrated flows, and debris flows, *in* Baker, V.R., Kochel, R.C., and Patton, C., eds., Flood Geomorphology: John Wiley, New York, p. 113–122.

D'Agostino, V., Cesca, M., and Marchi, L., 2010, Field and laboratory investigations of runout distances of debris flows in the Dolomites (Eastern Italian Alps): Geomorphology, v. 115, p. 294–304.

D'Arcy, M., Roda-Boluda, D.C., and Whittaker, A.C., 2017, Glacial–interglacial climate changes recorded by debris flow fan deposits, Owens Valley, California: Quaternary Science Reviews, v. 169, p. 288–311.

De Haas, T., and van Woerkom, T., 2016, Bed scour by debris flows: experimental investigation of effects of debris-flow composition: Earth Surface Processes and Landforms: v. 41, p. 1951–1966.

De Haas, T., Ventra, D., Carbonneau, P.E., and Kleinhans, M.G., 2014, Debris-flow dominance of alluvial fans masked by runoff reworking and weathering: Geomorphology, v. 217, p. 165–181.

De Haas, T., Braat, L., Leuven, J.F.W., Lokhorst, I.R., and Kleinhans, M.G., 2015a, Effects of debris-flow composition and topography on runout distance, depositional mechanisms and deposit morphology: Journal of Geophysical Research, Earth Surface, v. 120, p. 1949–1972.

De Haas, T., Ventra, D., Hauber, E., Conway, S.J., and Kleinhans, M.G., 2015b, Sedimentological analyses of Martian gullies: the subsurface as the key to the surface: Icarus, v. 258, p. 92–108.

De Haas, T., Kleinhans, M.G., Carbonneau, P.E., Rubensdotter, L., and Hauber, E., 2015c, Surface morphology of fans in the high-Arctic periglacial environment of Svalbard: controls and processes: Earth-Science Reviews, v. 146, p. 163–182.

De Haas, T., van den Berg, W., Braat, L., and Kleinhans, M.G., 2016, Autogenic avulsion, channelization and backfilling dynamics of debris-flow fans: Sedimentology, v. 63, p. 1596–1619.

De Haas, T., Densmore, A.L., Stoffel, M., Suwa, H., Imaizumi, F., Ballesteros-Cánovas, J.A., and Wasklewicz, T., 2018a, Avulsions and the spatio-temporal evolution of debris-flow fans: Earth-Science Reviews, v. 177, p. 53–75.

De Haas, T., Kruijt, A., and Densmore, A.L., 2018b, Effects of debris-flow magnitude-frequency distribution on avulsions and fan development: Earth Surface Processes and Landforms, v. 43, p. 2779–2793.

De Lange, S.I., Santa, N., Pudasaini, S.P., Kleinhans, M.G., and de Haas, T., 2020, Debris-flow generated tsunamis and their dependence on debris-flow dynamics: Coastal Engineering, v. 157, article 103623.

Deplus, C., Le Friant, A., Boudon, G., Komorowski, J.C., Villemant, B., Harford, C., Ségoufin, J., and Cheminée, J.L., 2001, Submarine evidence for large-scale debris

avalanches in the Lesser Antilles Arc: Earth and Planetary Science Letters, v. 192, p. 145–157.

Dufresne, A., Geertsema, M., Shugar, D.H., Koppes, M., Higman, B., Haeussler, P.J., Stark, C., Venditti, J.G., Bonno, D., Larsen, C., Gulick, S.P.S., McCall, N., Walton, M., Loso, M.G., and Willis, M.J., 2018, Sedimentology and geomorphology of a large tsunamigenic landslide, Taan Fiord, Alaska: Sedimentary Geology, v. 364, p. 302–318.

Dühnforth, M., Densmore, A.L., Ivy-Ochs, S., Allen, P.A., and Kubik, P.W., 2007, Timing and patterns of debris flow deposition on Shepherd and Symmes Creek fans, Owens Valley, California, deduced from cosmogenic ^{10}Be: Journal of Geophysical Research, v. 112, no. F03S15.

Fisher, R.V., 1971, Features of coarse-grained, high-concentration fluids and their deposits: Journal of Sedimentary Research, v. 41, p. 916–927.

George, D.L., Iverson, R.M., and Cannon, C.M., 2017, New methodology for computing tsunami generation by subaerial landslides: application to the 2015 Tyndall Glacier landslide, Alaska: Geophysical Research Letters, v. 44, p. 7276–7284.

Griswold, J.P., and Iverson, R.M., 2008, Mobility Statistics and Automated Hazard Mapping for Debris Flows and Rock Avalanches: U.S. Geological Survey, Scientific Investigation Report, 2007–5276.

Hart, K., Carey, S., Sigurdsson, H., Sparks, R.S.J., and Robertson, R.E., 2004, Discharge of pyroclastic flows into the sea during the 1996–1998 eruptions of the Soufrière Hills volcano, Montserrat: Bulletin of Volcanology, v. 66, p. 599–614.

Heidarzadeh, M., Muhari, A., and Wijanarto, A.B., 2019, Insights on the source of the 28 September 2018 Sulawesi tsunami, Indonesia based on spectral analyses and numerical simulations: Pure and Applied Geophysics, v. 176, p. 25–43.

Heller, V., 2011, Scale effects in physical hydraulic engineering models: Journal of Hydraulic Research, v. 49, p. 293–306.

Heller, V., Hager, W.H., and Minor, H.E., 2008, Scale effects in subaerial landslide generated impulse waves: Experiments in Fluids, v. 44, p. 691–703.

Herd, R.A., Edmonds, M., and Bass, V., 2006, Catastrophic lava dome failure at Soufrière Hills Volcano, Montserrat 12–13 July 2003: Journal of Volcanology and Geothermal Research, v. 148, p. 234–252.

Higman, B., Shugar, D.H., Stark, C.P., et al., 2018, The 2015 landslide and tsunami in Taan Fiord, Alaska: Scientific Reports, v. 8, p. 1–12.

Hoefling, R., 2004, High-speed 3D imaging by DMD technology, in Machine Vision Applications in Industrial Inspection XII: International Society for Optics and Photonics, Proceedings, p. 188–194, doi:10.1117/12.528341.

Hubert, J.F., and Filipov, A.J., 1989, Debris-flow deposits in alluvial fans on the west flank of the White Mountains, Owens Valley, California, USA: Sedimentary Geology, v. 61, p. 177–205.

Hughes, S.A., 1993, Advanced Series on Ocean Engineering 7: Physical Models and Laboratory Techniques in Coastal Engineering: London, World Scientific, 568 p.

Iverson, R.M., 1997, The physics of debris flows: Reviews of Geophysics, v. 35, p. 245–296.

Iverson, R.M., 2015, Scaling and design of landslide and debris-flow experiments: Geomorphology, v. 244, p. 9–20.

Iverson, R.M., Schilling, S.P., and Vallance, J.W., 1998, Objective delineation of lahar-inundation hazard zones: Geological Society of America, Bulletin, v. 110, p. 972–984.

Iverson, R.M., Logan, M., LaHusen, R.G., and Berti, M., 2010, The perfect debris flow? Aggregated results from 28 large-scale experiments: Journal of Geophysical Research, v. 115, no. F03005.

Jakob, M., 2005, Debris-Flow Hazard Analysis, Debris-Flow Hazards and Related Phenomena: Berlin, Springer, p. 411–443.

Johnson, C.G., Kokelaar, B.P., Iverson, R.M., Logan, M., LaHusen, R.G., and Gray, J.M.N.T., 2012, Grain-size segregation and levee formation in geophysical mass flows: Journal of Geophysical Research: Earth Surface, v. 117, no. F01032.

Kafle, J., Kattel, P., Mergili, M., Fischer, J.T., and Pudasaini, S.P., 2019, Dynamic response of submarine obstacles to two-phase landslide and tsunami impact on reservoir: Acta Mechanica, v. 230, p. 3143–3169.

Kim, B.C., and Lowe, D.R., 2004, Depositional processes of the gravelly debris flow deposits, South Dolomite alluvial fan, Owens Valley, California: Geosciences Journal, v. 8, p. 153–170.

Kurtz, D.D., and Anderson, J.B., 1979, Recognition and sedimentologic description of recent debris-flow deposits from the Ross and Weddell seas, Antarctica: Journal of Sedimentary Research, v. 49, p. 1159–1169.

Laberg, J.S., and Vorren, T.O., 1995, Late Weichselian submarine debris flow deposits on the Bear Island Trough mouth fan: Marine Geology, v. 127, p. 45–72.

Le Friant, A., Deplus, C., Boudon, G., Sparks, R.S.J., Trofimovs, J., and Talling, P., 2009, Submarine deposition of volcaniclastic material from the 1995–2005 eruptions of Soufrière Hills volcano, Montserrat: Journal of the Geological Society, v. 166, p. 171–182.

Macías, J.L., Espindola, J.M., Bursik, M., and Sheridan, M.F., 1998, Development of lithic breccias in the 1982 pyroclastic flow deposits of El Chichon volcano, Mexico: Journal of Volcanology and Geothermal Research, v. 83, p. 173–196.

Major, J.J., 1997, Depositional processes in large-scale debris-flow experiments: The Journal of Geology, v. 105, p. 345–366.

Major, J.J., and Iverson, R.M., 1999, Debris-flow deposition: effects of pore-fluid pressure and friction concentrated at flow margins: Geological Society of America, Bulletin, v. 111, p. 1424–1434.

Miller, G.S., Andy Take, W., Mulligan, R.P., and McDougall, S., 2017, Tsunamis generated by long and thin granular landslides in a large flume: Journal of Geophysical Research, Oceans, v. 122, p. 653–668.

Mitchell, N.C., Masson, D.G., Watts, A.B., Gee, M.J., and Urgeles, R., 2002, The morphology of the submarine flanks of volcanic ocean islands: a comparative study of the Canary and Hawaiian hotspot islands: Journal of Volcanology and Geothermal Research, v. 115, p. 83–107.

Mohammed, F., and Fritz, H.M., 2012, Physical modeling of tsunamis generated by three-dimensional deformable granular landslides: Journal of Geophysical Research, Oceans, v. 117, p. C11015.

Pierson, T.C., 1984, Why debris flows stop [Abstract]: Geological Society of America, Abstracts with Programs, v. 16, p. 623.

Prior, D.B., Bornhold, B.D., and Johns, M.W., 1984, Depositional characteristics of a submarine debris flow: The Journal of Geology, v. 92, p. 707–727.

Pudasaini, S.P., 2012, A general two-phase debris flow model: Journal of Geophysical Research, v. 117, no. F03010.

Pudasaini, S.P., 2014, Dynamics of submarine debris flow and tsunami: Acta Mechanica, v. 225, p. 2423–2434.

Pudasaini, S.P., 2019, A fully analytical model for virtual mass force in mixture flows: International Journal of Multiphase Flow, v. 113, p. 142–152.

Pudasaini, S.P., 2020, A full description of generalized drag in mixture mass flows: Engineering Geology, v. 265, no. 105429.

Pudasaini, S.P., and Fischer, J.T., 2020, A mechanical model for phase-separation in debris flow: International Journal of Multiphase Flow, v. 129, no. 103292.

Pudasaini, S.P., and Mergili, M., 2019, A multi-phase mass flow model: Journal of Geophysical Research: Earth Surface, v. 124, p. 2920–2942.

Pudasaini, S.P., and Miller, S.A., 2013, The hypermobility of huge landslides and avalanches: Engineering Geology, v. 157, p. 124–132.

Rickenmann, D., 1999, Empirical relationships for debris flows: Natural Hazards, v. 19, p. 47–77.

Schneider, J.L., Torrado, F.J.P., Torrente, D.G., Wassmer, P., Santana, M.D.C.C., and Carracedo, J.C., 2004, Sedimentary signatures of the entrance of coarse-grained volcaniclastic flows into the sea: the example of the breccia units of the Las Palmas Detritic Formation (Mio–Pliocene, Gran Canaria, Eastern Atlantic, Spain): Journal of Volcanology and Geothermal Research, v. 138, p. 295–323.

Schürch, P., Densmore, A.L., Ivy-Ochs, S., Rosser, N.J., Kober, F., Schlunegger, F., McArdell, B.W., Alfimov, V., 2016, Quantitative reconstruction of late Holocene surface evolution on an alpine debris-flow fan: Geomorphology, v. 275, p. 46–57.

Sohn, Y.K., Park, K.H., and Yoon, S.H., 2008, Primary versus secondary and subaerial versus submarine hydrovolcanic deposits in the subsurface of Jeju Island, Korea: Sedimentology, v. 55, p. 899–924.

Sparks, R.S.J., Gardeweg, M.C., Calder, E.S., and Matthews, S.J., 1997, Erosion by pyroclastic flows on Lascar Volcano, Chile: Bulletin of Volcanology, v. 58, p. 557–565.

Toyos, G., Dorta, D.O., Oppenheimer, C., Pareschi, M.T., Sulpizio, R., and Zanchetta, G., 2007, GIS-assisted modelling for debris flow hazard assessment based on the events of May 1998 in the area of Sarno, southern Italy: Part I: Maximum run-out, Earth Surface Processes and Landforms, v. 32, p. 1491–1502.

Trofimovs, J., Amy, L., Boudon, G., Deplus, C., Doyle, E., Fournier, N., Hart, M.B., Komorowski, J.C., Le Friant, A., Lock, E.J., Pudsey, C., Ryan, G., Sparks, R.S.J., and Pudsey, C., 2006, Submarine pyroclastic deposits formed at the Soufrière Hills volcano, Montserrat (1995–2003): What happens when pyroclastic flows enter the ocean?: Geology, v. 34, p. 549–552.

Trofimovs, J., Sparks, R.S.J., and Talling, P.J., 2008, Anatomy of a submarine pyroclastic flow and associated turbidity current: July 2003 dome collapse, Soufriere Hills volcano, Montserrat, West Indies: Sedimentology, v. 55, p. 617–634.

Urgeles, R., Canals, M., Baraza, J., Alonso, B., and Masson, D., 1997, The most recent megalandslides of the Canary Islands: El Golfo debris avalanche and Canary debris flow, west El Hierro Island: Journal of Geophysical Research, Solid Earth, v. 102, p. 20305–20323.

Vendettuoli, D., Clare, M.A., Clarke, J.H., Vellinga, A., Hizzet, J., Hage, S., Cartigny, M.J.B., Talling, P.J., Waltham, D., Hubbard, S.M., Stacey, C., and Lintern, D.G., 2019, Daily bathymetric surveys document how stratigraphy is built and its extreme incompleteness in submarine channels: Earth and Planetary Science Letters, v. 515, p. 231–247.

Wang, F.W., Zhang, Y.M., Huo, Z.T., Matsumoto, T., and Huang, B.L., 2004, The July 14, 2003 Qianjiangping landslide, Three Gorges reservoir, China: Landslides, v. 1, p. 157–162.

Received 19 February 2020; accepted 21 June 2020.